



Ultra-thin and near-unity selective emitter for efficient cooling

DO HYEON KIM,^{1,4}  GIL JU LEE,^{1,2,4}  SE-YEON HEO,¹ SOOMIN SON,³ KYEONG MUK KANG,¹ HEON LEE,^{3,5} AND YOUNG MIN SONG^{1,6} 

¹*School of Electrical Engineering and Computer Science, Gwangju Institute of Science and Technology, Cheomdangwagi-ro 123, Buk-gu, Gwangju 61005, Republic of Korea*

²*Department of Electronics Engineering, Pusan National University, Busandaehak-ro 63beon-gil 2, Geumjeong-gu 64241, Busan, Republic of Korea*

³*Department of Materials Science and Engineering, Korea University, Anam-ro 145, Seongbuk-gu, Seoul 02841, Republic of Korea*

⁴*These authors contributed equally to this work.*

⁵*heonlee@korea.ac.kr*

⁶*ymsong@gist.ac.kr*

Abstract: For the efficient radiative cooling of objects, coolers should emit heat within atmospheric transparent window and block heat absorption from the surrounding environments. Thus, selective emitters enable highly efficient cooling via engineered photonic structures such as metamaterials and multi-stacking structures. However, these structures require sophisticated fabrication processes and large quantities of materials, which can restrict mass-production. This study introduces an ultra-thin ($\sim 1\ \mu\text{m}$) and near-unity selective emitter (UNSE) within the atmospheric window, which can be fabricated using simple and affordable process. The combination of infrared (IR) lossy layers and high index lossless layer enhances the resonance in the structure thus, the emissivity in long wavelength IR region increases to near-unity within a thickness of $\sim 1\ \mu\text{m}$.

© 2021 Optical Society of America under the terms of the [OSA Open Access Publishing Agreement](#)

1. Introduction

Modern cooling systems primarily operate using fossil fuels and electricity. However, these systems consume nearly 20% of the global energy, which accelerates the depletion of fossil fuels [1]. Furthermore, rising demand for cooling aggravates environmental issues, such as air pollution and ozone depletion [2]. The growing awareness of the energy situation and environmental concerns has motivated the improvement of the efficiency of existing cooling systems and the pursuit of green-collar cooling technologies as new alternatives. Passive radiative cooling is an appealing concept for the 21st century, owing to energy-free and environmental sustainability [3–17], which can be applied to solar cells [18,19], textiles [20], building exteriors [21], fluids [22], colored cooling tiles [23], and space cooling [24,25]. High emissivity within the long wave infrared (LWIR; 8–13 μm) region of the atmospheric transparent window enables heat dissipation ($\sim 300\ \text{K}$) to outer space (*i.e.*, Universe; 3 K) without any energy consumption or pollutant emission [26].

For high cooling efficiency, selective emission in the LWIR region (*i.e.*, 8–13 μm) is essential to prevent undesirable heat gains from the atmosphere and surrounding environment (*i.e.*, building and ground) through the outside LWIR region (*i.e.*, $< 8\ \mu\text{m}$ and $> 13\ \mu\text{m}$) while emitting heat in the LWIR region [26]. In particular, such spectral selectivity benefits urban areas, where have many discouragements such as building for efficient thermal radiation to outer space [27]. Thus, recent research has yielded a variety of passive selective emitter (SE) designs comprising sophisticated emissive coatings, such as photonic structures, meta-materials, and multi-stacking

(>5 layers) structures [28–36]. Although efficient, these designs are costly, owing to the need for a large quantities of material and complicated fabrication technology, which can restrict mass-production.

Here, we propose an ultra-thin/near-unity selective emitter (UNSE), amenable to low-cost/large-scale fabrication. Overall layouts of the UNSE comprise a high-index lossless layer (HILL; Ge) and IR lossy layers (SiO_2 and Si_3N_4). Combining a HILL with the highly absorbent layers in the LWIR region remarkably enhances IR emission, owing to light trapping at the lossy layers. On the basis of its exceptional optical sensitivity with phase changes in the structure, the proposed structure is optimized at an ultra-thin thickness ($\sim 1.1 \mu\text{m}$) compared with the thermal wavelength ($\sim 10 \mu\text{m}$). We also computationally demonstrate the cooling efficiency of major cities in the world using practical weather conditions (*i.e.*, climates and averaged ambient temperatures in summer and winter) to demonstrate the cooling powers and temperature of the proposed structure. This result confirms that our UNSE exhibits thermoregulation features where the UNSE has higher and lower cooling powers in summer and winter, respectively, compared with the ideal broadband emitter. Furthermore, we achieved daytime cooling by laminating the solar opaque/IR transparent layer (SOIT), which can be self-assembled on the UNSE.

2. Results and discussion

2.1. Basic concept of Ultra-thin/near-unity selective emitter

Our proposed UNSE is shown in **Fig. 1(a)**; the figure exhibits enhanced emission using a HILL on a conventional-selective emitter (C-SE; composed of lossy layers) and the corresponding scanning electron microscope (SEM) image of the fabricated sample. The proposed UNSE consists of a tri-layer (*i.e.*, one HILL and two IR lossy layers) on a metal substrate. Because the HILL has a high refractive index in the IR region, the light at the lossy layers, between the HILL and metal substrate, is trapped, which enhances IR absorption (*i.e.*, emission) at lossy layers. The SEM image shows the fabricated UNSE, which comprises Ge (125 nm) as the HILL, SiO_2 (280 nm) and Si_3N_4 (650 nm) as lossy layers, and a metal reflector comprising an Al film (30 nm) deposited on a silicon substrate. Although UNSE was optimized by using Ge, SiO_2 , and Si_3N_4 layers in this study, other lossless materials which possess high-index of refraction (*i.e.*, Si, GaAs, ZnS, and BaF_2) can replace the Ge layer as HILL (**Figure S1** in [Supplement 1](#)). Thus, any high-index lossless materials in IR region can be used to design the UNSE, which can overcome the limitations such as fabrication cost. Moreover, various IR lossy materials such as SiC, HfO_2 , TiO_2 , and Al_2O_3 , can also comprise UNSE as lossy layers (**Figure S2** in [Supplement 1](#)). These computational studies demonstrate the universality of the concept of HILL on IR lossy layers for strong LWIR emission with ultra-thin thickness ($\sim 1 \mu\text{m}$) and only a few resonant layers (3 to 4 layers). **Figure 1(b)** shows the optical image of the fabricated 4-inch sized UNSE, demonstrating the feasibility of large-scale fabrication (**Fig. 1(b)**). As shown in **Fig. 1(c)**, two dielectrics (*i.e.*, SiO_2 and Si_3N_4) are utilized as IR lossy media because these materials are absorptive in LWIR region (*i.e.*, 8–13 μm). Ge is a promising candidate for the HILL since it has a high refractive index (~ 4) and a nearly zero extinction coefficient (< 0.01) in the IR region, which enhances resonance at the lossy layers.

The absorption profiles were simulated to investigate the emissivity enhancement phenomenon of the UNSE as the absorption may be equal to emissivity by Kirchhoff's law (**Fig. 1(d)**). Compared with the C-SE, the combination of the HILL with the C-SE induces the enhancement of absorption at wavelengths of 9.5 and 10.5 μm , which are the high absorptive regions of the SiO_2 and Si_3N_4 . Although absorption also occurs in the C-SE, owing to the high extinction coefficients of lossy layers, the absorption is significantly enhanced by the additional HILL to trap the incident light in the UNSE. Thus, the UNSE exhibits an increased emission, especially in the LWIR region (**Fig. 1(e)**). The emissivity of the UNSE is higher than C-SE in the LWIR region while emissivity is still low outside the LWIR region. As the atmosphere is also transparent in the

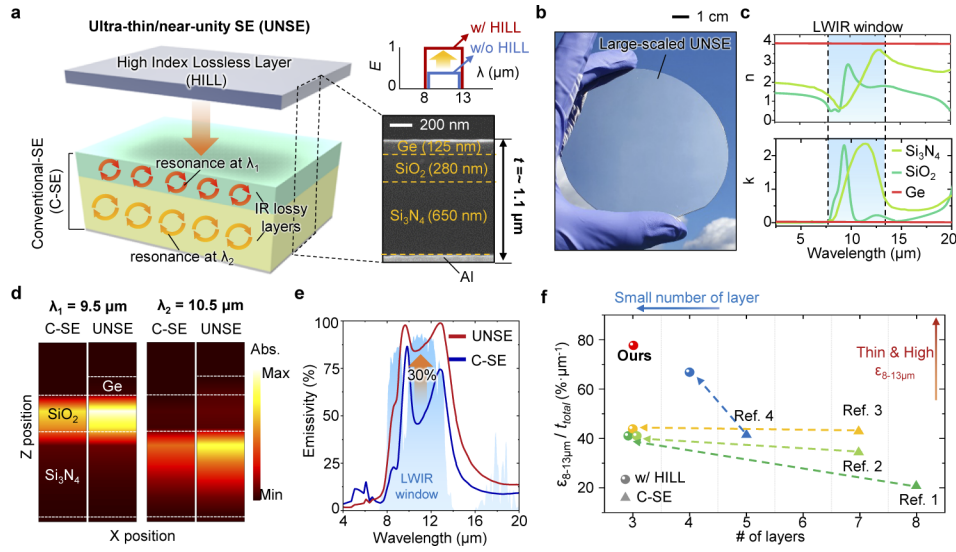


Fig. 1. (a) Schematic of an ultra-thin/near-unity selective emitter (UNSE) composed of conventional-SE (C-SE) and high index lossless layer (HILL), exhibiting light trapping which enhances IR emission by high index lossless layer (HILL). The scanning electron microscope (SEM) of fabricated UNSE with thickness information. (b) The optical image of fabricated 4-inch sized UNSE. (c) Refractive indices (top) and extinction coefficients (bottom) for materials, composed of UNSE (*i.e.*, Ge, SiO₂, and Si₃N₄). (d) Absorption profiles of conventional-selective emitter (C-SE) and UNSE at 9.5 and 10.5 μm wavelength, where the largest absorption occurs in SiO₂ and Si₃N₄ respectively. (e) Calculated emissivity spectra of UNSE and C-SE in the 4 to 20 μm wavelength region. (f) Average emissivity in LWIR region ($\epsilon_{8-13\mu\text{m}}$) per total thickness (t_{total}) with the number of layers ($\#_{\text{layers}}$) of our UNSE (SiO₂, Si₃N₄, Ge), Ref. 1 (SiO₂, TiO₂), Ref. 2 (TiO₂, SiO₂), Ref. 3 (SiO₂, HfO₂), Ref. 4 (TiO₂, SiO₂, Si₃N₄), and redesigned UNSE of reported C-SE with additional HILL (*i.e.*, Ge).

range of 16–26 μm in some regions (e.g., high latitude area), slight increasing emissivity within that range can enhance the cooling performance. However, we focused on the LWIR region (8–13 μm) since the atmospheric transparent window is totally opaque within the range of 16–26 μm in the areas where cooling is mostly demanded (e.g., mid-latitude and tropical region).

Compared with other selective emitters (Fig. 1(f); triangular symbols) in previous literature, our optimized structure (Fig. 1(f); red colored circular symbol) exhibits the highest average emissivity in the LWIR area ($\epsilon_{8-13\mu\text{m}}$) per total thickness (t_{total}). Moreover, the emissivity per thickness of conventional emitters (Fig. 1(f); triangular symbols) can be significantly enhanced by redesigning the structures (Fig. 1(f); circular symbols) with an additional HILL (*i.e.*, Ge) while the numbers of layers are reduced. In particular, the emissivity per total thickness of Ref. 1 [28] is increased from 21% to 41% with decreasing the number of layers from 8 to 3. Thus, these results indicate that the combination of HILL and conventional lossy layers (*i.e.*, SiO₂, Si₃N₄, TiO₂, and HfO₂) can improve the emissivity with reducing the thickness and the number of layers. Detailed information on these selective emitters is provided in **Figure S3** and **Table S1** in [Supplement 1](#).

2.2. HILL for high selective emission

For efficient cooling, HILL should enhance the emissivity within the LWIR region while avoiding the emissivity rise outside the LWIR region. To increase the emissivity selectively in the LWIR

region with thickness variation, the reflection coefficient trajectories are analyzed. By calculating the reflection coefficient trajectories and emissivity spectra of the C-SE and UNSE, we analyze the effects of the HILL (i.e., Ge) on the emissivity of the UNSE (**Fig. 2**). The geometrical values of the C-SE were optimized by comparing the averaged emissivity in the LWIR region within the total thickness of $0.9\ \mu\text{m}$ for a thin and efficient SE design (**Figure S4a** in **Supplement 1**). **Figure 2(a)** shows the reflection coefficients of the C-SE and UNSE at different wavelengths within (i.e., $\lambda = 9.5$ and $11.5\ \mu\text{m}$; center points of LWIR region) and outside of the LWIR region (i.e., $\lambda = 6$ and $15\ \mu\text{m}$). As shown in **Fig. 2(a)**, the trajectory differs by variation of layers (dot line: Si_3N_4 , dash line: SiO_2 , and solid line: Ge) and thicknesses. The end points of trajectory for each structure are presented as spherical shapes (red and blue). In the diagram, the x-axis and y-axis present the real and imaginary terms of reflection coefficient respectively and the spacing between major grids is 0.2. The reflection coefficient diagram gives the information of reflectance variation by calculating the distance from zero. Therefore, when the reflection coefficient is close to zero, the reflectance is also near zero. Because the UNSE does not allow any transmission owing to a sufficiently thick Al substrate, low reflectance is equal to high emissivity. Compared with the C-SE, a thin Ge layer ($125\ \text{nm}$) enables a reduction in the reflectance ($R < 30\%$) in the LWIR region, which indicates the high emissivity (i.e., $E > 70\%$). On the other hand, the emissivity is only minimally enhanced outside the LWIR region. As shown in **Figure S5a** and **S5b** in **Supplement 1**, there is a limit to achieving prominent selective emission with only thicknesses regulation of Si_3N_4 and SiO_2 in thin thickness ($< 1\ \mu\text{m}$). Because Ge has a high refractive index in the IR region, the reflection coefficient changes more significantly with the variation in thickness of the Ge layer than that with Si_3N_4 and SiO_2 . Thus, the combination of the Ge layer enables emissivity enhancement for the ultra-thin thickness (**Figure S5c** in **Supplement 1**).

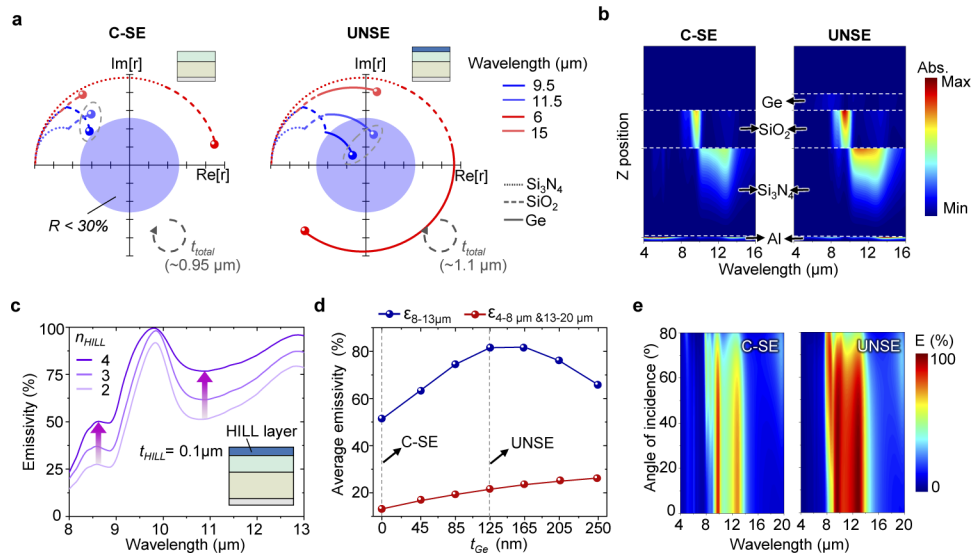


Fig. 2. (a) Reflection coefficient trajectory of the C-SE and UNSE for the total thickness (t_{total}) at different wavelength regions (inside the LWIR region: 9.5 and $11.5\ \mu\text{m}$ and outside LWIR region: 6 and $15\ \mu\text{m}$). The x-axis and y-axis show the real and imaginary terms of reflection coefficient respectively. (b) Absorption profiles of the C-SE and UNSE as a function of wavelength (i.e., $4\text{--}16\ \mu\text{m}$). (c) Calculated emissivity spectra of the UNSE with different refractive indices of the HILL (n_{HILL}). (d) Average emissivity inside (i.e., $8\text{--}13\ \mu\text{m}$) and outside the LWIR (i.e., $4\text{--}8\ \mu\text{m}$ and $13\text{--}20\ \mu\text{m}$) as a function of Ge thickness (t_{Ge}). (e) Calculated angular response of the C-SE and UNSE up to the incident angle of 80° .

Figure 2(b) presents the absorption profiles of the C-SE and UNSE as a function of wavelength, which highlights the emissivity enhancement of the UNSE. The C-SE exhibits absorption in the LWIR region, owing to the IR lossy layers (i.e., SiO₂ and Si₃N₄). Since Ge layer has a high refractive index (~ 4) and a nearly zero extinction coefficient in the IR region, the transmitted light through the HILL is trapped in the IR lossy layers, which elongates the optical path. As shown in Fig. 1(c), SiO₂ and Si₃N₄ are almost absorptive in the LWIR region, whereas nearly zero absorption occurs in other region. Thus, increased optical path causes enhanced absorption in the LWIR region; however, absorption is barely enhanced in other regions. For this reason, absorption is only enhanced in the LWIR region in the UNSE.

Figure 2(c) presents the emissivity spectra for different refractive indices of the HILL, which has an extinction coefficient of zero. As a higher refractive index causes multiple reflections, more incident light is trapped in the lossy layers, which enhances the emissivity of the LWIR region. Therefore, Ge, which has a high refractive index (~ 4), is a promising candidate for the HILL. Figure 2(d) shows the average emissivity inside (i.e., $\epsilon_{8-13\mu\text{m}}$) and outside of the LWIR region (i.e., $\epsilon_{4-8\mu\text{m}\&14-20\mu\text{m}}$) as a function of the Ge thickness. Average emissivity is highest at a thickness of 125 nm since that condition exhibits the point closest to zero in the reflection coefficient diagram (Fig. 2(a) and Figure S5c). Since the thicker HILL enhances the multiple reflection in lossy layers, the emissivity increases with higher thickness of HILL. However, above the thickness of 125 nm decreases the $\epsilon_{8-13\mu\text{m}}$ as the amount of trapped light in the lossy layers is reduced due to the impedance mismatching. Because the extinction coefficient of Si₃N₄ also exists within 14–20 μm , $\epsilon_{4-8\mu\text{m}\&14-20\mu\text{m}}$ slightly increase; however, the gap between emissivity (i.e., $\epsilon_{8-13\mu\text{m}} - \epsilon_{4-8\mu\text{m}\&14-20\mu\text{m}}$) is also the highest at 125 nm. Therefore, this condition ($t_{\text{Ge}} = 125 \text{ nm}$) is selected for optimization, which satisfies with the condition of maximizing the heat emission while minimizing the heat gain. Figure 2(e) presents the simulated emissivity of the C-SE and UNSE as a function of the incident angle. A notable emission peak shift and phase change are not observed in both the C-SE and UNSE (Figure S6 in Supplement 1) as the incident angle increases. This result indicates that an additional Ge layer does not crucially affect the emissivity degradation at high incident angles. Such angle-independency can be explained by the considerably thin total thickness of the UNSE compared with the thermal wavelength (i.e., $\sim 10 \mu\text{m}$). Fundamentally, optical resonators with sub-wavelength thickness have notable angle-robustness, due to their negligible phase shift at an oblique incident angle [37–39].

2.3. Cooling performances of UNSE in various conditions

To analyze the cooling efficiency of the optimized structure, we calculate the cooling temperature and cooling power under various conditions (i.e., dry/humid and windless/windy) using the thermal equilibrium equation:[21]

$$P_{\text{rad}}(T_{\text{sam}}) - P_{\text{Sun}} - P_{\text{atm}}(T_{\text{amb}}) + h_c(T_{\text{sam}} - T_{\text{amb}}) = 0, \quad (1)$$

where $P_{\text{rad}}(T_{\text{sam}})$ is the radiative power of the sample per unit area at sample temperature (T_{sam}), P_{Sun} is the solar power absorbed to the sample per unit area, $P_{\text{atm}}(T_{\text{amb}})$ is the absorbed power from the atmosphere per unit area at ambient air temperature (T_{amb}), and $h_c(T_{\text{sample}} - T_{\text{ambient}})$ is the non-radiative heat exchange power (i.e., conduction and convection).

Figure 3(a) shows the calculated cooling temperature (T_{cool}) and the temperature difference between the ambient air and sample (i.e., $T_{\text{amb}} - T_{\text{sam}}$) of the UNSE and C-SE, respectively, in terms of LWIR opacity and the non-radiative heat exchange coefficient, h_c . In this calculation, the mid-latitude sky transmission model which is calculated using MODTRAN 6 software is used (Figure S7b in Supplement 1) for night time situation (i.e., $P_{\text{Sun}} = 0$). LWIR opacity is related to humidity since the sky transmittance decreases as the ambient gets humid [40]. The cooling temperatures of the UNSE ($T_{\text{cool,UNSE}}$) and C-SE ($T_{\text{cool,C-SE}}$) were calculated in the range of $7 < h_c < 10 \text{ W/m}^2/\text{K}$ to consider practical situations. The cooling temperature of the UNSE is

always higher than that of the C-SE for different h_c and LWIR opacities. Because the radiative power (P_{rad}) of the UNSE is always higher than that of C-SE owing to a higher $\epsilon_{8-13\mu m}$, while P_{atm} is the same for both, the cooling temperature of the UNSE is always higher than that of the C-SE. This result indicates that the cooling performance of the UNSE is better, even in humid or windy weather (*i.e.*, $h_c \sim 10$). Figure 3(b) shows the enhancement of the cooling temperature in terms of the cooling temperature ratio (*i.e.*, $T_{cool,UNSE}/T_{cool,C-SE}$) as a function of h_c . As h_c increases, the cooling temperature ratio increases to approximately 150% compared to that of the C-SE. This result indicates that the UNSE has a better cooling performance difference in practical situations (*i.e.*, $h_c > 5$) compared with the ideal case (*i.e.*, $h_c \sim 0$).

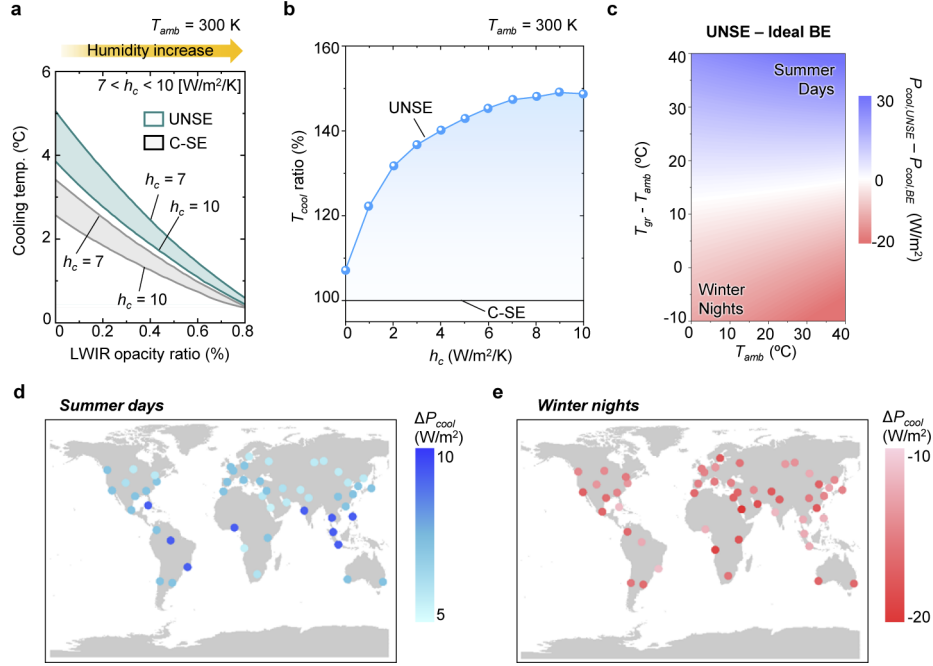


Fig. 3. (a) Calculated cooling temperature (T_{cool}) of the UNSE and C-SE as a function of LWIR opacity. The non-radiative heat transfer coefficient (h_c) ranges between 7–10 W/m²/K for the consideration of a practical situation. (b) Calculated cooling temperature ratio (*i.e.*, $T_{cool, ratio} = T_{cool,UNSE}/T_{cool,C-SE}$) with a variation of h_c . (c) Differences between P_{cool} of an UNSE and ideal BE as a function of ambient air temperature (T_{amb}) and ground temperature (T_{gr}). (d,e) Worldwide distribution of the cooling potential difference between the UNSE and ideal BE (*i.e.*, $\Delta P_{cool} = P_{cool,UNSE} - P_{cool,BE}$) in (d) summer and (e) winter.

Conventionally, broadband emitter (BE; 4–20 μm) is widely used for cooling devices owing to their facile fabrication and abundant materials [41–44]. Thus, demonstrating the advantages of our UNSE over BE is essential. An ideal SE particularly benefits urban areas, where much heat is emitted from surrounding environments (*i.e.*, buildings and structures) compared with the ideal BE [24]. To analyze this effect, we estimate the cooling power with consideration to these conditions using the revised thermal equation:[27]

$$P_{cool} = (I_{emitter} - vI_{sky}) - (1 - v)I_{earth}, \quad (2)$$

where P_{cool} is the cooling power of the emitter, $I_{emitter}$ is the irradiance of the emitter at T_{amb} , I_{sky} is the atmospheric irradiance (T_{amb}), I_{earth} is the radiation from the ground or surrounding environments (T_{gr}), and v is the view factor (≤ 0.5). The detailed information of revised equation is described in **Materials and methods**.

As shown in Fig. 3(c), the UNSE achieves greater P_{cool} than an ideal BE in the case of summer days (*i.e.*, $T_{amb} < T_{gr}$; ground temperature). In this calculation, v is fixed to 0.25 to confirm the cooling efficiency in urban areas, where many buildings exist. Since the UNSE shows selective emission in the 8–13 μm range, the external heat from the surrounding environments (I_{earth}) is reduced compared with broadband emitter; however, the amount of heat emission does not reduce (Figure S8a, b in Supplement 1). Therefore, the UNSE exhibits better cooling performance in summer days than BE. Conversely, when $T_{amb} > T_{gr}$, $P_{cool,UNSE}$ is lower than that of BE, which prevents undesirable heat loss in the cold condition. As the broadband emitter loses more heat to sub-ambient objects than the selective emitter, BE exhibits higher cooling power in the cold case (Figure S8c, d). Therefore, the UNSE exhibits better cooling performance in summer but a lower performance in winter compared with BE. This result demonstrates the thermoregulation feature of the UNSE compared with BE.

For practical global urban cases, the cooling power is calculated worldwide in summer and winter considering geographical locations (e.g., desert, subarctic, temperate, and tropical) and meteorological conditions (e.g., average temperatures and humidity) (Fig. 3(d), e). The regional climate data is based on the Köppen climate classification which considers the elevation, annual precipitation, and annual temperature (Figure S9 in Supplement 1) [45]. Meteorological data, such as the average temperatures and atmospheric transparency are from the National Centers for Environmental Information (NOAA) [46] and calculated from MODTRAN software respectively (Figure S7). In order to confirm the tendencies of the cooling power globally, several cities are selected as major urban areas in each continent (Table S2-7 in Supplement 1). The cooling powers of each region are calculated using the average summer and winter temperatures of each region (Table S2-7 in Supplement 1) and atmospheric transmission data (Figure S7) based on the Köppen climate. Figure 3(d) shows the distribution of the cooling power difference (ΔP_{cool}) between the UNSE and Ideal BE ($P_{cool,UNSE} - P_{cool,BE}$) in hot conditions (*i.e.*, summer days). The ground temperature is set to be higher than the ambient temperature (*i.e.*, $T_{gr} = T_{amb} + 20$ °C), which represents hot summer days. Summer sky transmissions of each climate type are used for calculation (Figure S7 in Supplement 1). The cooling power of the UNSE tends to be entirely higher (>5 W/m²) than that of the BE during the summer season when cooling is most in demand. Besides, the potential gap is larger (~ 10 W/m²), particularly in tropical regions, where cooling is more essential. Since the sky transmission of tropical regions is narrower than that of other regions, the cooling power difference between SE and BE is larger (Figure S8a in Supplement 1).

Whereas higher cooling performance in summer, lower cooling powers are found in the winter season (Fig. 3(e)). In contrast to the summer case, the ground temperature is set to be lower than the ambient temperature (*i.e.*, $T_{gr} = T_{amb} - 5$ °C), which represents cold winter nights. Winter sky transmissions of each climate type are used for calculation (Figure S7). As the ground temperature is lower than ambient temperature, heat loss occurs by surrounding environments (I_{earth}) whereas heat gain occurs from the surroundings in summer. Thus, SE loses less heat than BE (Figure S8b), which indicates a lower cooling power in the world map (< -10 W/m²) totally. The cooling power difference is larger in high latitude regions compared with tropical regions, owing to the narrower sky transmission of tropical regions (Figure S8b). Consequently, our UNSE exhibits a better cooling effect under hot conditions (*i.e.*, summer days) and a better insulation effect under cold conditions (*i.e.*, winter days) compared with BE. The absolute cooling potentials of the UNSE and Ideal BE are presented in Figure S10 in Supplement 1.

2.4. Day-time cooling capability with SOIT

For day-time cooling, achieving high solar reflection is as essential as selective emission. Although the UNSE has high selective emission in IR region, absorption occurs in the solar region as Ge is absorptive in the visible range. Therefore, we propose an approach to enhance cooling efficiency in the daytime by combining a SOIT with the UNSE (Fig. 4(a)). To achieve high solar reflection

and IR transmission for the SOIT, a porous IR transparent polymer is demanded (e.g., porous styrene ethylene butylene styrene (p-SEBS) and porous polyethylene (PPE)) as they show high solar reflectance and IR transmittance [47]. Among them, p-SEBS film, which is IR transparent ($> 80\%$) at a thin thickness ($\sim 100 \mu\text{m}$), is used since p-SEBS has higher solar reflectance and IR transparent feature than PPE at thin thickness (**Figure S11** in **Supplement 1**). Figure 4(a) displays its optical image and SEM image. The fabrication process of the porous SEBS is described in the **Materials and methods**. Because micro-sized air pores ($\sim 1 \mu\text{m}$) cause light scattering in SEBS, which enhances solar reflection, porous SEBS optically presents a white color which indicates high reflectivity in the visible range [47, 48]. As shown in Fig. 4(b), the Al plate pattern can be observed using an IR camera, even in the case of a SOIT on the Al plate, while the pattern is invisible to naked eye because SOIT is visibly opaque. Thus, this result proves the IR transparency of the fabricated SOIT. Figure 4(c) shows the measured emissivity spectra of the UNSE, SOIT combined with the UNSE (SOIT-UNSE), and SOIT. The UNSE exhibits high emissivity in the visible range (Fig. 4(c); left), which hinders daytime cooling. The SOIT-UNSE shows significantly lower emissivity ($< 10\%$) than the UNSE in the solar spectrum. In addition, combining the SOIT with the UNSE does not reduce the IR emissivity. Therefore, these optical characteristics justify day-time cooling since SOIT-UNSE satisfies high solar reflection and emission. The detailed information for measurement of emissivity are described in **Materials and methods**.

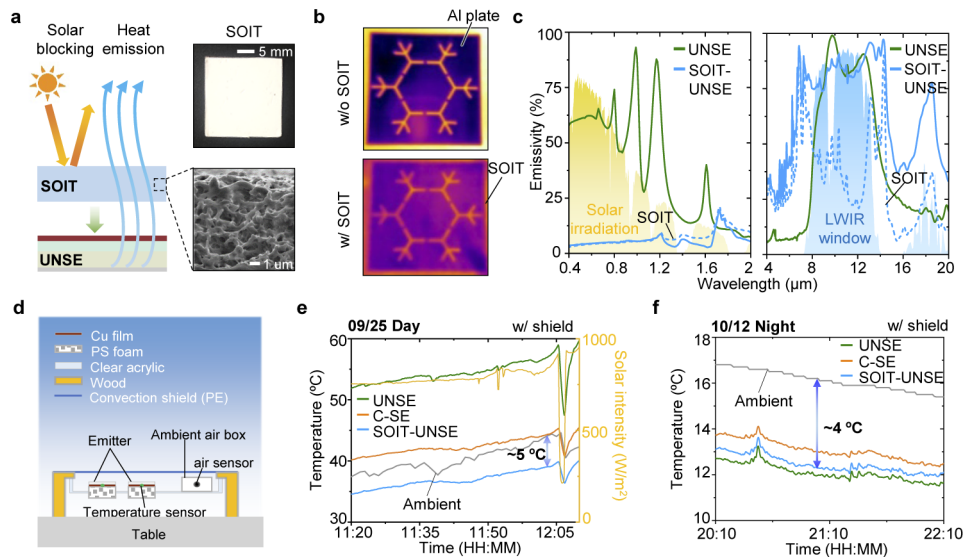


Fig. 4. (a) Schematic illustration of the approach to achieve day-time cooling via SOIT with an SEM image and optical image of a fabricated SOIT (i.e., porous SEBS). (b) Thermal images of a patterned Al plate and a SOIT combined with an Al plate. (c) Measured emissivity spectra of the UNSE, SOIT-UNSE, and SOIT in the visible (left) and IR range (right). (d) Schematic illustration of the cooling temperature measurement setup. (e and f) Temperature measurement of the UNSE, C-SE, and SOIT-UNSE during the (e) day and (f) night.

Figure 4(d) presents the scheme of the measurement setup. A convection shield (low-density polyethylene; LDPE) is used to measure the temperature at a low non-radiative coefficient, h_c . In addition, polystyrene (PS) foam is used to reduce the effects of non-radiative heat transfer (i.e., conduction and convection). Moreover, copper films were placed between the emitter and temperature sensor to minimize the temperature gradients of the samples. Figure 4(e) and 4(f)

present the outdoor temperature measurements for day and night, respectively. By integrating with the SOIT, SOIT-UNSE has an increased cooling capability of $\sim 5^{\circ}\text{C}$ sub-ambient cooling during daytime since the solar reflectance is greatly higher compared with the UNSE. Furthermore, both SOIT-UNSE and UNSE exhibit a cooling performance of $\sim 4^{\circ}\text{C}$ sub-ambient cooling in night. In the night-time result, temperature peaks of samples were resulted from sudden change in cloud volume or wind speed. Probably, because an abrupt change in ambient air temperature was not found, the reason for the temperature peaks might be expected by cloud shading. The cloud can block the radiative heat transfer from the radiative coolers to the universe, hence it can increase the temperature of samples. The cooling temperature trends of the samples are in good agreement with the calculated trends (**Figure S12** in [Supplement 1](#)). The measurement results for several days (**Figure S13** in [Supplement 1](#)) and the weather conditions (**Table S8**) such as wind speed and relative humidity are presented in [Supplement 1](#).

3. Conclusion

In this study, we presented an ultra-thin, highly selective emitter by combining a HILL, which enables light trapping in the structure. Optical analysis characteristics, such as the reflection coefficient and absorption profile, provide a design rule for the optimum UNSE. The emissivity of the optimized UNSE increased ($>80\%$) in the range of $8\text{--}13\text{ }\mu\text{m}$, whereas the emissivity is low ($<20\%$) in the other wavelength range. The simulated results prove that the optimized structure has a better cooling capability than the C-SE, even in humid and windy weather conditions. Furthermore, the UNSE has a thermoregulation capability compared with BE. Finally, we proved the high cooling efficiency via measurement. By combining the UNSE and SOIT, $\sim 5^{\circ}\text{C}$ and $\sim 4^{\circ}\text{C}$ sub-ambient cooling is achieved in day-time and night-time, respectively. These successful demonstrations indicate that our proposed structure can be applied to cool the temperatures of heat-sensitive and high-power electronics. Moreover, the proposed configuration, *i.e.*, the integration of a highly selective/near-unity selective emitter and solar opaque/IR reflection layer, can provide a new low-cost, scalable, and highly efficient radiative cooling approach.

4. Materials and methods

Optical simulation: To simulate the emissivity spectra of several structures, rigorous coupled wave analysis-based commercial software (DiffractionMOD, RSoft Design Group, Synopsys, USA) was employed. Absorption profiles were also simulated using this software. In all the simulations, a 0.5 nm -square grid size was utilized to numerically calculate the stable emissivity. The complex refractive index dispersions for materials (*i.e.*, SiO_2 , Si_3N_4 , and Ge) were considered to obtain accurate spectral results. The refractive indices were obtained from previously published results [49,50]. The Drude model was used for the optical constants of Al.

Characterization: The emissivity spectra were characterized by measuring the reflectance spectra of the samples using a Fourier transform infrared spectrometer (Spectrum Paragon, Perkin Elmer, Inc., USA) with an Au-coated integrating sphere to detect the diffuse reflection. Because the infrared rays cannot pass through even a thin Al layer, the emissivity spectra were derived from the measured reflectance spectra (*i.e.*, $E = 1 - R$). SEM (S-4700, Hitachi Hi-Technologies, Japan) was utilized to observe the cross-section of the fabricated UNSE.

Measurement: For the thermal imaging, the Al plate was placed on a hot plate at a temperature of 40°C with and without the SOIT. A thermal camera (E6, FLIR Systems, Inc., USA) captured the sample surface. For the radiative cooling temperature measurement, Cu foils were attached to the back surfaces of the samples and were of the same sizes as the samples. Between the samples and Cu foils, temperature sensors (ST-50, RKC Instrument Inc., Japan) were inserted and connected to a data logger (RDXL6SD, Omega Engineering, USA). An ambient air temperature sensor was inserted in an Al box to prevent solar heating and measure the temperature of the naturally convective air.

Thermal equilibrium equation: The thermal equilibrium equation, $P_{rad}(T_{sample}) - P_{Sun} - P_{atm}(T_{ambient}) + P_{non-rad} = 0$, is composed of the following four terms:

$$P_{rad}(T_{sample}) = \int_0^{2\pi} \int_0^{\frac{\pi}{2}} \int_0^{\infty} I_{BB}(T_{sample}, \lambda) \epsilon(\lambda, \theta) \cos(\theta) \sin(\theta) d\lambda d\theta d\phi \quad (3)$$

$$P_{atm}(T_{ambient}) = \int_0^{2\pi} \int_0^{\frac{\pi}{2}} \int_0^{\infty} I_{BB}(T_{ambient}, \lambda) \epsilon(\lambda, \theta) \epsilon_{amb}(\lambda, \theta) \cos(\theta) \sin(\theta) d\lambda d\theta d\phi \quad (4)$$

$$P_{sun} = \int_0^{\infty} I_{AM1.5G}(\lambda) \epsilon(\lambda, \theta) d\lambda \quad (5)$$

$$P_{non-rad} = h_c(T_{sample} - T_{ambient}). \quad (6)$$

Here, $I_{BB} = (2hc^2/\lambda^5)/[e^{\frac{hc}{\lambda k_B T}} - 1]$ is the spectral radiance of a blackbody at temperature T , where h , c , k_B , and λ , and h_c are Planck's constant, the velocity of light, the Boltzmann constant, wavelength, and the non-radiative heat exchange coefficient, respectively. The atmospheric emissivity is given by $\epsilon_{amb}(\lambda, \theta) = 1 - t(\lambda)^{1/\cos(\theta)}$, where t is the sky transmission calculated utilizing MODTRAN 6 with the conditions of an urban site at mid-latitude in summer and winter.

Revised thermal equation: The revised thermal equation for cooling potential, $P_{cool} = (I_{emitter} - \nu I_{sky}) - (1 - \nu)I_{earth}$, is composed of the following three terms:

$$I_{emitter} = \int_0^{2\pi} \int_0^{\frac{\pi}{2}} \int_0^{\infty} I_{BB}(T_{ambient}, \lambda) \epsilon(\lambda, \theta) \cos(\theta) \sin(\theta) d\lambda d\theta d\phi \quad (7)$$

$$I_{sky} = \int_0^{2\pi} \int_0^{\frac{\pi}{2}} \int_0^{\infty} I_{BB}(T_{ambient}, \lambda) \epsilon(\lambda, \theta) \epsilon_{amb}(\lambda, \theta) \cos(\theta) \sin(\theta) d\lambda d\theta d\phi \quad (8)$$

$$I_{earth} = \int_0^{2\pi} \int_0^{\frac{\pi}{2}} \int_0^{\infty} I_{BB}(T_{ground}, \lambda) \epsilon(\lambda, \theta) \cos(\theta) \sin(\theta) d\lambda d\theta d\phi \quad (9)$$

Here, $I_{BB} = (2hc^2/\lambda^5)/[e^{\frac{hc}{\lambda k_B T}} - 1]$ is the spectral radiance of a blackbody at temperature T , where h , c , k_B , and λ are Planck's constant, the velocity of light, the Boltzmann constant, and wavelength, respectively. The term ν is the view factor (≤ 0.5) [27].

Porous SEBS fabrication: SEBS (3.5 weight % (wt %); Tuftec H1062, Asahi Kasei, Japan) was mixed with 81 wt % chloroform (C2432, Sigma-Aldrich; solvent) and 15.5 wt % isopropanol alcohol in a test tube at room temperature (300 K). The solution was then sonicated for a day to completely dissolve the SEBS particles. After sonication, the solution was placed on a glass slide and dried for a day so that it could harden.

Funding. National Research Foundation of Korea (NRF-2021R1C1C2013605, 2018M3D1A1058997, 2020R1A2C2004983); Korea Institute of Energy Technology Evaluation and Planning (KETEP) and the Ministry of Trade, Industry & Energy (MOTIE) of the Republic of Korea (20183010014310); GIST Research Institute (GRI) grant.

Disclosures. The authors declare that there are no conflicts of interest related to this article.

Data availability. Data underlying the results presented in this paper are not publicly available at this time but may be obtained from the authors upon reasonable request.

Supplemental document. See Supplement 1 for supporting content.

References

1. T IEA, The Future of Cooling, www.iea.org/reports/the-future-of-cooling, accessed: May, 2018.
2. IEA, Cooling—Tracking Clean Energy Process, www.iea.org/tcep/buildings/cooling, accessed: Oct., 2019.
3. J. Jaramillo-Fernandez, G. L. Whitworth, J. A. Pariente, A. Blanco, P. D. Garcia, C. Lopez, and C. M. Sotomayor-Torres, "A Self-Assembled 2D Thermofunctional Material for Radiative Cooling," *Small* **15**(52), 1905290 (2019).
4. H. Zhang, K. C. S. Ly, X. Liu, Z. Chen, M. Yan, Z. Wu, X. Wang, Y. Zheng, H. Zhou, and T. Fan, "Biologically inspired flexible photonic films for efficient passive radiative cooling," *Proc. Natl. Acad. Sci.* **117**(26), 14657–14666 (2020).
5. A. P. Raman, M. A. Anoma, L. Zhu, E. Rephaeli, and S. Fan, "Passive radiative cooling below ambient air temperature under direct sunlight," *Nature* **515**(7528), 540–544 (2014).
6. L. Zhu, A. Raman, and S. Fan, "Color-preserving daytime radiative cooling," *Appl. Phys. Lett.* **103**(22), 223902 (2013).
7. X. Sun, Y. Sun, Z. Zhou, M. A. Alam, and P. Bermel, "Radiative sky cooling: fundamental physics, materials, structures, and applications," *Nanophotonics* **6**(5), 997–1015 (2017).

8. J.-L. Kou, Z. Jurado, Z. Chen, S. Fan, and A. J. Minnich, "Daytime radiative cooling using near-black infrared emitters," *ACS Photonics* **4**(3), 626–630 (2017).
9. S. Atiganyanun, J. B. Plumley, S. J. Han, K. Hsu, J. Cytrynbaum, T.L. Peng, S. M. Han, and S. E. Han, "Effective radiative cooling by paint-format microsphere-based photonic random media," *ACS Photonics* **5**(4), 1181–1187 (2018).
10. J. Mandal, Y. Fu, A. C. Overvig, M. Jia, K. Sun, N. N. Shi, H. Zhou, X. Xiao, N. Yu, and Y. Yang, "Hierarchically porous polymer coatings for highly efficient passive daytime radiative cooling," *Science* **362**(6412), 315–319 (2018).
11. J. Song, J. Seo, J. Han, J. Lee, and B. J. Lee, "Ultrahigh emissivity of grating-patterned PDMS film from 8 to 13 μm wavelength regime," *Appl. Phys. Lett.* **117**(9), 094101 (2020).
12. S. Jeon and J. Shin, "Ideal spectral emissivity for radiative cooling of earthbound objects," *Sci. Rep.* **10**(1), 1–7 (2020).
13. X. Yin, R. Yang, G. Tan, and S. Fan, "Terrestrial radiative cooling: Using the cold universe as a renewable and sustainable energy source," *Science* **370**(6518), 786–791 (2020).
14. M. H. Kang, G. J. Lee, J. H. Lee, M. S. Kim, Z. Yan, J.-W. Jeong, K.-I. Jang, and Y. M. Song, "Outdoor-Useable, Wireless/Battery-Free Patch-Type Tissue Oximeter with Radiative Cooling," *Adv. Sci.* **8**(2004), 885 (2021).
15. Z. F. Mira, S.-Y. Heo, D. H. Kim, G. J. Lee, and Y. M. Song, "Multilayer selective passive daytime radiative cooler optimization utilizing memetic algorithm," *J. Quant. Spectrosc. Radiat. Transfer* **272**(1), 107774 (2021).
16. Z. Chen, L. Zhu, A. Raman, and S. Fan, "Radiative cooling to deep sub-freezing temperatures through a 24-h day–night cycle," *Nat. Commun.* **7**(1), 1–5 (2016).
17. H. Yuan, C. Yang, X. Zheng, W. Mu, Z. Wang, W. Yuan, Y. Zhang, C. Chen, X. Liu, and W. Shen, "Effective, angle-independent radiative cooler based on one-dimensional photonic crystal," *Opt. Express* **26**(21), 27885–27893 (2018).
18. L. Zhu, A. Raman, K. X. Wang, M. A. Anoma, and S. Fan, "Radiative cooling of solar cells," *Optica* **1**(1), 32–38 (2014).
19. B. Zhao, M. Hu, X. Ao, and G. Pei, "Performance analysis of enhanced radiative cooling of solar cells based on a commercial silicon photovoltaic module," *Sol. Energy* **176**, 248–255 (2018).
20. P.-C. Hsu and X. Li, "Photon-engineered radiative cooling textiles," *Science* **370**(6518), 784–785 (2020).
21. T. Li, Y. Zhai, S. He, W. Gan, Z. Wei, M. Heidarinejad, D. Dalgo, R. Mi, X. Zhao, J. Song, J. Dai, C. Chen, A. Aili, A. Vellore, A. Martini, R. Yang, J. Srebric, X. Yin, and L. Hu, "A radiative cooling structural material," *Science* **364**(6442), 760–763 (2019).
22. D. Zhao, A. Aili, Y. Zhai, J. Lu, D. Kidd, G. Tan, X. Yin, and R. Yang, "Subambient cooling of water: Toward real-world applications of daytime radiative cooling," *Joule* **3**(1), 111–123 (2019).
23. G. J. Lee, Y. J. Kim, H. M. Kim, Y. J. Yoo, and Y. M. Song, "Colored, daytime radiative coolers with thin-film resonators for aesthetic purposes," *Adv. Opt. Mater.* **6**(22), 1800707 (2018).
24. S.-Y. Heo, G. J. Lee, D. H. Kim, Y. J. Kim, S. Ishii, M. S. Kim, T. J. Seok, B. J. Lee, H. Lee, and Y. M. Song, "A Janus emitter for passive heat release from enclosures," *Sci. Adv.* **6**(36), eabb1906 (2020).
25. D. H. Kim, G. J. Lee, S.-Y. Heo, il-Suk Kang, and Y. M. Song, "Thermostat property of Janus emitter in enclosures," *Sol. Energy Mater. Sol. Cells* **230**(1), 111173 (2021).
26. H.-Y. Chan, S. B. Riffat, and J. Zhu, "Review of passive solar heating and cooling technologies," *Renewable Sustainable Energy Rev.* **14**(2), 781–789 (2010).
27. J. Mandal, S. Mandal, J. Brewer, A. Ramachandran, and A. P. Raman, "Radiative Cooling and Thermoregulation in the Earth's Glow," arXiv, submitted: Jun., (2020), Available at: <https://arxiv.org/abs/2006.11931>.
28. R. Eden, A. Raman, and S. Fan, "Ultrabroadband photonic structures to achieve high-performance daytime radiative cooling," *Nano Lett.* **13**(4), 1457–1461 (2013).
29. M. M. Hossain, B. Jia, and M. Gu, "A metamaterial emitter for highly efficient radiative cooling," *Adv. Opt. Mater.* **3**(8), 1047–1051 (2015).
30. K. Yao, H. Ma, M. Huang, H. Zhao, J. Zhao, Y. Li, S. Dou, and Y. Zhan, "Near-Perfect Selective Photonic Crystal Emitter with Nanoscale Layers for Daytime Radiative Cooling," *ACS Appl. Nano Mater.* **2**(9), 5512–5519 (2019).
31. S. Y. Jeong, C. Y. Tso, J. Ha, Y. M. Wong, C. Y. H. Chao, B. Huang, and H. Qiu, "Field investigation of a photonic multi-layered TiO₂ passive radiative cooler in sub-tropical climate," *Renewable Energy* **146**(1), 44–55 (2020).
32. D. Chae, M. Kim, P. H. Jung, S. Son, J. Seo, Y. Liu, B. J. Lee, and H. Lee, "Spectrally selective inorganic-based multilayer emitter for daytime radiative cooling," *ACS Appl. Mater. Interfaces* **12**(7), 8073–8081 (2020).
33. L. Fan, W. Li, W. Jin, M. Orenstein, and S. Fan, "Maximal nighttime electrical power generation via optimal radiative cooling," *Opt. Express* **28**(17), 25460–25470 (2020).
34. J.-Y. Wu, Y.-Z. Gong, P.-R. Huang, G.-J. Ma, and Q.-F. Dai, "Diurnal cooling for continuous thermal sources under direct subtropical sunlight produced by quasi-Cantor structure," *Chin. Phys. B* **26**(10), 104201 (2017).
35. G. J. Lee, D. H. Kim, S.-Y. Heo, and Y. M. Song, "Spectrally and Spatially Selective Emitters Using Polymer Hybrid Spoof Plasmonics," *ACS Appl. Mater. Interfaces* **12**(47), 53206–53214 (2020).
36. N. F. Cunha, A. AL-Rjoub, L. Rebouta, L. G. Vieira, and S. Lanceros-Mendez, "Multilayer passive radiative selective cooling coating based on Al/SiO₂/SiNx/SiO₂/TiO₂/SiO₂ prepared by dc magnetron sputtering," *Thin Solid Films* **694**, 137736 (2020).
37. Y. J. Yoo, J. H. Lim, G. J. Lee, K.-I. Jang, and Y. M. Song, "Ultra-thin films with highly absorbent porous media fine-tunable for coloration and enhanced color purity," *Nanoscale* **9**(9), 2986–2991 (2017).

38. Y. J. Yoo, J. H. Ko, W.-G. Kim, Y. J. Kim, D.-J. Kong, S. Kim, J.-W. Oh, and Y. M. Song, "Dual-Mode Colorimetric Sensor Based on Ultrathin Resonating Facilitator Capable of Nanometer-Thick Virus Detection for Environment Monitoring," *ACS Appl. Nano Mater.* **3**(7), 6636–6644 (2020).
39. J. H. Ko, Y. J. Yoo, Y. J. Kim, S.-S. Lee, and Y. M. Song, "Flexible, Large-Area Covert Polarization Display Based on Ultrathin Lossy Nanocolumns on a Metal Film," *Adv. Funct. Mater.* **30**(11), 1908592 (2020).
40. M. Dong, N. Chen, X. Zhao, S. Fan, and Z. Chen, "Nighttime radiative cooling in hot and humid climates," *Opt. Express* **27**(22), 31587–31598 (2019).
41. Y. Zhai, Y. Ma, S. N. David, D. Zhao, R. Lou, G. Tan, R. Yang, and X. Yin, "Scalable-manufactured randomized glass-polymer hybrid metamaterial for daytime radiative cooling," *Science* **355**(6329), 1062–1066 (2017).
42. B. Bhatia, A. Leroy, Y. Shen, L. Zhao, M. Gianello, D. Li, T. Gu, J. Hu, M. Soljacic, and E. N. Wang, "Passive directional sub-ambient daytime radiative cooling," *Nat. Commun.* **9**(1), 5001–5008 (2018).
43. A. Aili, Z. Y. Wei, Y. Z. Chen, D. L. Zhao, R. G. Yang, and X. B. Yin, "Selection of polymers with functional groups for daytime radiative cooling," *Mater. Today Phys.* **10**(1), 100127 (2019).
44. J. Mandal, Y. Yang, N. Yu, and A. P. Raman, "Paints as a scalable and effective radiative cooling technology for buildings," *Joule* **4**(7), 1350–1356 (2020).
45. D. Chen and H. W. "Using the Köppen classification to quantify climate variation and change: An example for 1901–2010," Chen," *Environmental Development* **6**(1), 69–79 (2013).
46. NOAA, National Centers for Environmental Information, www.ncdc.noaa.gov, accessed: Oct., 2020.
47. A. Leroy, B. Bhatia, C. C. Kelsall, A. Castillejo-Cuberos, M. D. Capua, L. Zhao, L. Zhang, and A. M. Guzman, "High-performance subambient radiative cooling enabled by optically selective and thermally insulating polyethylene aerogel," *Sci. Adv.* **5**(10), eaat9480 (2019).
48. Y. Xu, B. Sun, Y. Ling, Q. Fei, Z. Chen, X. Li, P. Guo, N. Jeon, S. Goswami, Y. Liao, S. Ding, Q. Yu, J. Lin, G. Huang, and Z. Yan, "Multiscale porous elastomer substrates for multifunctional on-skin electronics with passive-cooling capabilities," *Proc. Natl. Acad. Sci.* **117**(1), 205–213 (2020).
49. J. Kischkat, S. Peters, B. Gruska, M. Semtsiv, M. Chashnikova, M. Klinkmüller, O. Fedosenko, S. Machulik, A. Aleksandrova, G. Monastyrskyi, Y. Flores, and W. T. Masselink, "Mid-infrared optical properties of thin films of aluminum oxide, titanium dioxide, silicon dioxide, aluminum nitride, and silicon nitride," *Appl. Opt.* **51**(28), 6789–6798 (2012).
50. T. Amotchkina, M. Trubetskov, D. Hahner, and V. Pervak, "Characterization of e-beam evaporated Ge, YbF₃, ZnS, and LaF₃ thin films for laser-oriented coatings," *Appl. Opt.* **59**(5), A40–A47 (2020).